# Footprint geometry and sessile drop resonance

Chun-Ti Chang, Susan Daniel, and Paul H. Steen

Phys. Rev. E **95**, 033109 — Published 15 March 2017

DOI: 10.1103/PhysRevE.95.033109

# Footprint Geometry and Sessile Drop Resonance

Chun-Ti Chang*[1], Susan Daniel†[2], and Paul H. Steen‡[2]

[1]Department of Mechanical Engineering, National Taiwan University, Taipei 16017, Taiwan

[2]School of Chemical and Biomolecular Engineering, Cornell University, Ithaca, NY 14853, USA

February 21, 2017

**Abstract**

In this work, we experimentally examine the resonance of a sessile drop with a square footprint (square drop) on a flat plate. Two families of modal behaviors are reported. One family is identified with the modes of sessile drops with circular footprints (circular drop), denoted as 'spherical modes'. The other family is associated with Faraday waves on a square liquid bath (square Faraday waves), denoted as 'grid modes'. The two families are distinguished based on their dispersion behaviors. By comparing the occurrence of the modes, we recognize spherical modes as the *characteristic* of sessile drops and grid modes as the *constrained response*. Within a broader context, we further discuss the resonance modes of circular sessile drops and free spherical drops, and we recognize various modal behaviors as surface waves under different extents of constraint. From these, we conclude that sessile drops resonate according to how wavenumber selection by footprint geometry and capillarity compete. For square drops, a dominant effect of footprint constraint leads to grid modes; otherwise the drops exhibit spherical modes, the characteristic of sessile drops on flat plates.

*cc836@cornell.edu
†sd386@cornell.edu
‡phs7@cornell.edu

# 1 Introduction

Dynamics of sessile drops attracts much scientific interest for its significance in various applications [1–7]. Thanks to the progress in surface engineering, surfaces can now be treated with wetting patterns of great specificity, sharp contrast and excellent resolution [8–10]. This opens the door for greater droplet control in microfluidic and low-gravity applications. Here we investigate the fundamental dynamics of vibrated sessile drops, and we examine the influence of geometrical footprint constraint on the influence of sessile drop resonance.

The studies of resonating sessile drops on flat plates [11, 12] and Faraday waves [13] are similar in many aspects. For both, typical observables are mode shapes [11, 14–32], resonance frequencies [11, 14–32], and the evolution of surface waves with forcing amplitude [18, 23, 29–31, 33–35]. The free surface waves oscillate at the forcing frequency (harmonically) when the forcing acceleration is low. However, an elevated acceleration triggers modes which oscillate at half the forcing frequency [15, 18, 19, 21, 30–32], called half-frequency subharmonic modes. This has been identified as a parametric response, often modeled by the Mathieu-Hill equation [15, 18, 19, 25, 31, 32, 36, 37]. These common features apparently imply that resonance of drops and Faraday waves are closely related, although they have been separate studies in the literature mostly.

For resonating sessile drops, the dynamics of surface deflection has been modeled as the small-amplitude free response of a drop of ideal liquid with inertia distorting and capillarity restoring. Motions satisfy a Bernoulli equation in the bulk with kinematic and pressure conditions on the deformable surface. Using the boundary-integral approach the problem is mapped to the surface domain of a spherical cap rest state. On that domain, deflection curvature is related to pressure by the standard normal stress condition (Young-Laplace). Constant surface tension is assumed. An integro-differential operator equation results that represents the competition between liquid inertia and capillarity. This is a wave equation. The dispersive part involves a Laplace-Beltrami operator, essentially a surface Laplacian with non-constant coefficients that encode the rest-state curvatures. (For a planar rest state, the Laplace-Beltrami operator reduces to the classical Laplace operator.) This model has proved successful in capturing resonant frequencies for driven sessile drops that are not too flat [12,21,22]. These standing waves, pinned along circular footprints, are therefore classified using the spherical harmonic

symmetries inherited from free spherical drop oscillations [38,39]. We shall refer to these waves as Rayleigh capillary waves. The resonant response can either be harmonic or subharmonic.

For Faraday waves, the Benjamin-Ursell model [37] introduces the driving displacement as a periodic acceleration appearing in the body force term. The resulting equation is a modified wave equation with time-dependent coefficients - leading to the Mathieu-Hill model upon reduction. Later, Kumar and Tuckerman [40] perform a linear stability analysis of the weakly viscous problem. Zhang and Vañils [41] derive the quasi-potential equations for the weakly nonlinear problem and solve for the pattern selection near onset. The extents of validity in assuming weak viscosity and weak nonlinearity are recently examined [42, 43]. Additionally, the Faraday problem is placed in a nonlinear context and the rest state is shown to be stable for forcing of small enough amplitude. As forcing amplitude increases, the free surface wave bifurcates to subharmonic temporal behavior [44]. The nature of the bifurcation depends on the depth of the liquid bath [44]. Our interest here is in how Faraday waves change to Rayleigh capillary waves as droplet depth (volume) and footprint geometry are varied. We shall distinguish families of modal behaviors using traditional dispersion relationship tests, and we report experimental results.

The scopes of Rayleigh and Faraday studies are somewhat different. For example, Faraday waves have been examined for flat free surfaces in containers with circular and square footprints, conforming to cylindrical and rectangular coordinate geometries. As figure 1 summarizes, the corresponding eigenmodes are Bessel-Fourier and 2D Fourier series, respectively [37]. For sessile drops, published works typically utilize homogeneous flat substrates [15–17, 19, 21], on which a drop forms a spherical cap with a circular footprint. For such capillary spherical caps, the only known family of eigenmodes consists of those related to spherical harmonics [12]. For Faraday waves, varying the boundary geometry of the liquid bath changes the eigenmodes from Bessel-Fourier to 2D Fourier series. A curious question is then raised: how does a sessile drop resonate if its contact line is constrained to be square but its free surface curves somewhat like a spherical cap? More fundamentally, how do the effects of footprint geometry and free-surface curvature compete to determine the drop's resonance behavior?

In this work, we experimentally investigate the forced resonance of sessile drops with a square footprint (square drops). We constrain a sessile drop's footprint to be square on a flat

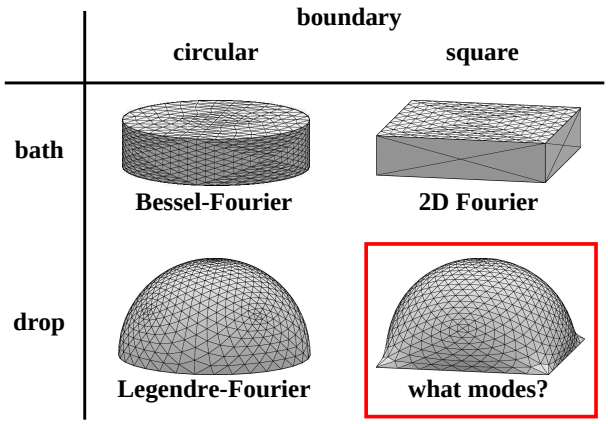


Figure 1: (Color online) Modes on the free surfaces of liquid baths and sessile drops for circular and square boundary symmetries. Motivating question of this work: What are the modes of a vibrated sessile drop with a square footprint?

plate, mechanically oscillate the plate, and observe the drop's resonance through high-speed imaging. The observations are compared to studies of sessile drops with a circular footprint (circular drop) and Faraday waves with a square boundary (square Faraday wave). It turns out that a square drop can exhibit two distinct families of modes depending on its volume: spherical and grid modes. In what follows, shape and frequency responses of the modes are presented first. Then a discussion on how dispersion distinguishes the modes of the two families follows. Finally, the natures of the different families of modes are identified.

## 2 Experimental Setup

Square and circular drops are tested with the same approach as in our previous works [21, 22]. Figure 2 shows our oscillation platform and observation apparatus. In experiments, our sessile drops are vertically oscillated by single-frequency sine waves on a VTS-100 mechanical vibrator (by Vibration Testing Systems, Aurora, OH, USA). Each sine wave is generated by an Agilent 33220A function generator (Agilent Technologies, SantaClara,CA) and then amplified by a Crown CE2000 power amplifier (Crown Audio, Elkhart, IN) before sending to the mechanical vibrator. Mirrors are installed to visualize drop motion using one high-speed camera (RedLake HG-XL, by Integrated Design Tools, Inc., Tallahassee, FL, USA). A woven metal mesh (product # 85385T875, from McMaster-Carr, Elmhurst, IL, USA) is sandwiched under the solid substrate that holds the drop. The wires of the mesh are approximately 60$\mu$m in diameter, and the openings are about 110 $\mu$m by 110 $\mu$m. Light is projected directly from underneath

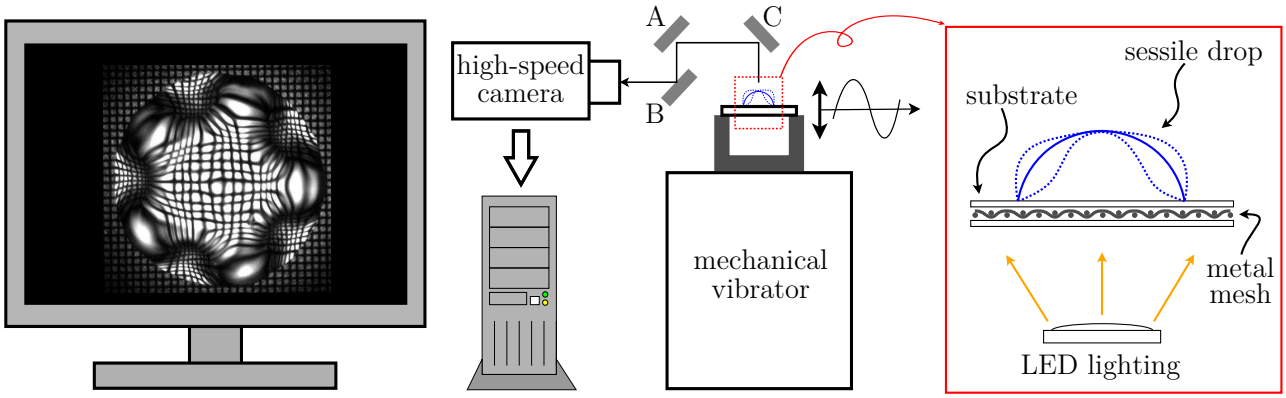


Figure 2: (Color online) Schematic of our experimental platform [21, 22]. Shown in the red (rightmost) box are the key components: mesh pattern and LED light source under the drop. Light rays from LEDs are refracted by the drop's deforming surface, reflected into the high-speed camera by mirrors A, B, and C, and convey a deformed mesh pattern to the computer, thereby visualizing the deformation of the drop's surface. A signal generator (not shown) oscillates the surface sinusoidally in the direction perpendicular to the plane of the surface.

the mesh. The drop surface refracts the light according to how the surface deforms and the so-deformed mesh is viewed from the top. The optics provides spatial resolutions of 10$\mu$m/pixel at 5000 frames per second and 15$\mu$m/pixel at 10470 frames per second. Features down to 40$\mu$m can be clearly resolved on the platform. Further detail may be found in [21].

For the experiments, each glass substrate is prepared with a relatively hydrophilic pinning footprint to constrain the footprint of a sessile drop. The relative hydrophilicity of a pinning footprint makes our drops stay pinned within the footprint area. Two glass substrates are prepared, one with a circular pinning footprint and the other a square one. The circular pinning footprint is 5 mm in diameter, and the square one has the same area as the circular one. Having the same wetted areas enables direct comparison of observations for drops of the same volume. Pure water drops of 10 - 30 $\mu$L are tested. The volume increment is 2 $\mu$L. The range of volumes ensures that our square drops fully cover the pinning footprint and stay pinned. In this work, each reported test is repeated at least 3 times to ensure reproducibility.

In what follows, a square, circular or sessile drop is termed *large* if it is larger than 20 $\mu$L, *small* if smaller than 16 $\mu$L, and *medium* if between 16 and 20 $\mu$L. For circular drops, the contact angle is 42° at 10$\mu$L, 60° at 16$\mu$L, 70° at 20$\mu$L and 86° at 30$\mu$L. Once deposited, a drop is mechanically oscillated and observed through high-speed imaging.

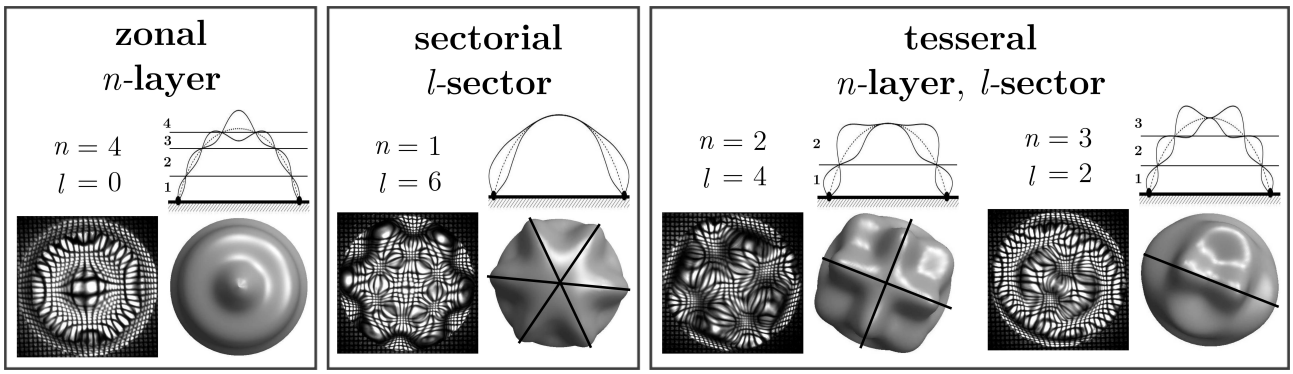


Figure 3: Examples of a zonal, a sectoral and two tesseral modes identified by their number of layer(s) $n$ and number of sector(s) $l$ [22]. For each mode, the side-view profile on the upper right and the top-view surface on the lower right are predicted by Bostwick-Steen theory [12]. The image on the lower left is experimental top-view snapshot of the mode [22].

# 3 Spherical Modes

Our large and medium square drops (subscript $s$) resonate like circular drops. For circular drops, our prior work has identified the first 37 modes according to their numbers of layers and sectors [22]. As figure 3 shows, layers and sectors are most recognizable in side and top views, respectively. *Zonal* modes consist of $n \geq 2$ axisymmetric layers. Axisymmetry means $l = 0$ sectors. For example, the illustrated $(n, l) = (4, 0)$ mode has four layers and no longitudinal variation. *Sectoral* modes have $n = 1$ layer with $l$ sectors. As an example, the (1, 6) mode exhibits $n = 1$ layer with $l = 6$ sectors. Finally, *tesseral* modes possess some ($l > 0$) longitudinal variation in multiple ($n > 1$) layers. The (2, 4) mode possesses $n = 2$ layers from the side view and $l = 4$ sectors from the top view. Likewise, $n = 3$ and $l = 2$ can be deduced from the side and top views of the (3, 2) mode. These are natural modes on spherical caps [12] and are denoted as *spherical modes*. In what follows, we present the features common to large and medium square drops. Then we identify these observed modes with spherical modes on circular drops.

Figure 4 shows the spherical modes examined in our experiments. A video of these modes is supplied in our supplementary materials [45]. The top row of figure 4 shows 3 spherical modes on circular drops. The modes are (1, 2), (1, 3) and (1, 4) according to our layer-sector naming convention [22]. A (1, 2) has 2 rotationally symmetric sectors in one layer. The bar shape of the (1, 2) is clearly recognizable as indicated by the solid line. A (1, 3) exhibits three rotationally symmetric sectors in one layer and appears like a $\Delta$ (or a $\bigtriangledown$). Finally, a (1, 4) possesses four sectors in one layer. The four-fold symmetry makes its pattern resemble a diamond, a square

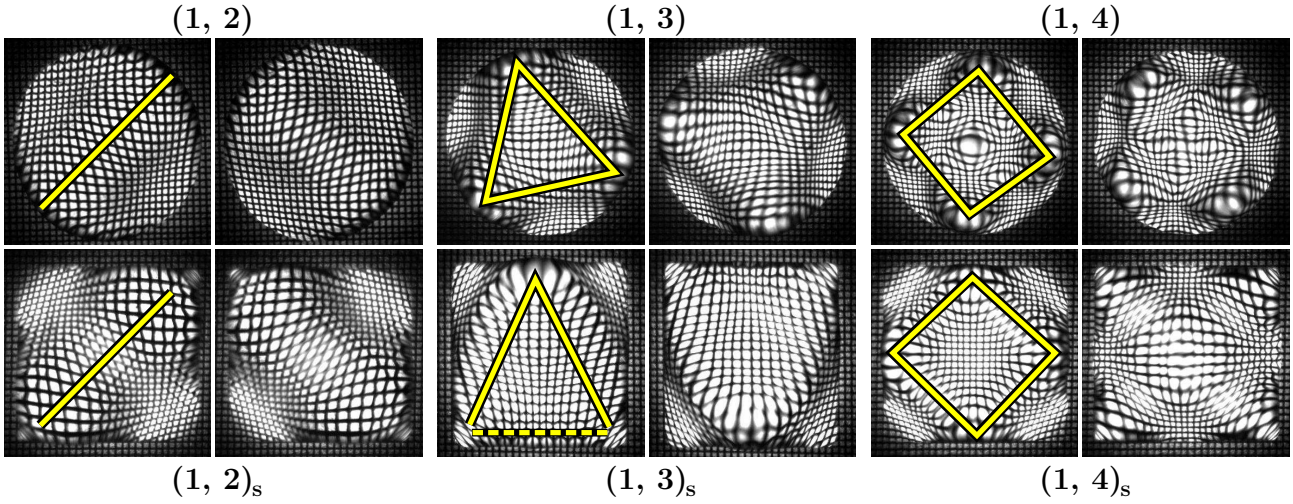


| mode | (1, 2) | $(1, 2)_s$ | (1, 3) | $(1, 3)_s$ | (1, 4) | $(1, 4)_s$ |
|---|---|---|---|---|---|---|
| volume ($\mu$L) | 20 | 24 | 22 | 24 | 16 | 20 |
| frequency(Hz) | 135 | 103 | 184 | 177 | 269 | 248 |
| acceleration(g) | 3 | 2.5 | 5 | 4 | 7 | 6 |

Figure 4: (Color online) Top-view snapshots of circular footprint (top row) and square footprint (bottom row) mode shapes, with two columns per mode comparing full-period and half-period shapes. The represented modes are (1, 2), $(1, 2)_s$, (1, 3), $(1, 3)_s$, (1, 4) and $(1, 4)_s$. Corresponding forcing frequencies and accelerations in table below. As a guide to the eye, yellow bars superimposed to highlight symmetry of mode shapes. The footprints of circular drops are 5mm in diameter. Each edge of a square drop's footprint is 4.43mm. A video of these modes is supplied in the supplementary materials [45].

or a cross.

Large and medium square drops exhibit similar mode shapes. In figure 4, $(1, 2)_s$ exhibits a diagonal, bar-shaped ridge which is identical to the pattern of a (1, 2). With a $(1, 4)_s$, a square drop shows either a diamond-shaped pattern or a cross. In either case, the four-fold symmetry of $(1, 4)_s$ resembles the pattern of a (1, 4). For $(1, 3)_s$, the $\Lambda$-shaped (or V-shaped) pattern is missing a third ridge to complete a $\Delta$ (or a $\bigtriangledown$). The third ridge is suspected to submerge close to the drop's bottom (top) edge, and the pinning at the drop's edge presumably inhibits its appearance. Hence, on the basis of figure 4 alone, an association of (1, 3) and $(1, 3)_s$ is unclear. To make a positive association of these two modes, one needs to inspect their frequency bands, introduced below.

A difference between (1, 2), (1, 3), (1, 4) and $(1, 2)_s$, $(1, 3)_s$, $(1, 4)_s$ is how these modes can orient their patterns. This is perhaps not obvious from figure 4, as we have chosen snapshots of modes with similar orientations to demonstrate their shape similarity. For (1, 2), (1, 3) and (1, 4), we see almost any orientation of the patterns. However, the patterns of $(1, 2)_s$, $(1, 3)_s$ and

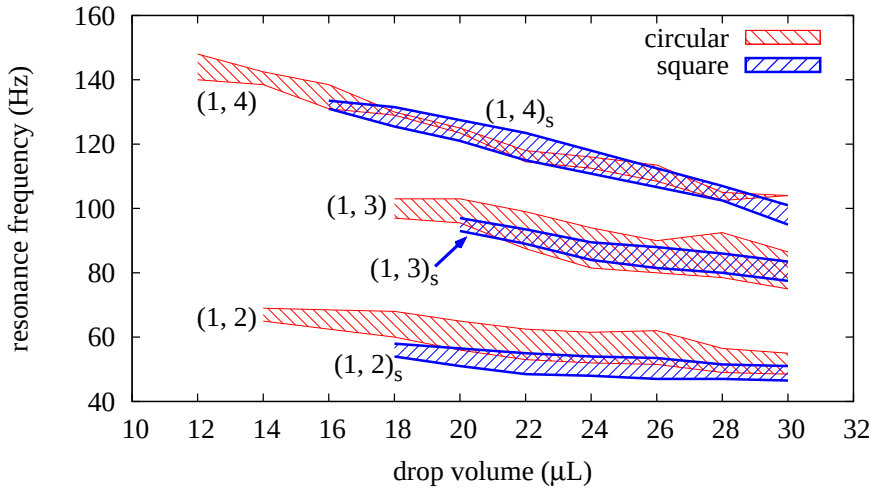


Figure 5: (Color online) Measured frequency bands of circular and square footprint modes as volume varies: (1, 2), $(1, 2)_s$, (1, 3), $(1, 3)_s$, (1, 4) and $(1, 4)_s$ modes.

$(1, 4)_s$ are fixed. In experiments, the bar-shaped ridges of $(1, 2)_s$ are always diagonal. For $(1, 3)_s$, the tip of its $\Lambda$ (or V) always lies in the middle of an edge. That is, a $(1, 3)_s$ always 'rocks' parallel to edges of the footprint, not diagonally. Finally, the diamond pattern of a $(1, 4)_s$ in the left snapshot always differs from the footprint by 45°, and the cross in the right snapshot must match the footprint's both diagonals. Apparently the orientations of $(1, 2)_s$, $(1, 3)_s$ and $(1, 4)_s$ are constrained by the symmetry of the drop's square footprint.

Figure 5 shows the frequency bands of the modes in figure 4. In experiments, the modes appear within a finite window of frequencies. Outside this window, mode shapes are not observed. Therefore, we probe the lower and upper observed frequencies. These are the upper and lower limits of the frequency bands in figure 5. For example, $(1, 3)_s$ oscillates between 80 and 86 Hz on a 28$\mu$L square drop, and (1, 3) between 97 and 103 Hz on an 18 $\mu$L square drop. The maximum volume of our drops is constrained by apparatus to 30 $\mu$L. The minimum volume below which modes cease to appear depends on the mode. The bands terminate at different volumes. Importantly, we probed the frequencies of all six modes for drops down to 10$\mu$L. However, $(1, 2)_s$ is observed only for drops at least 18$\mu$L, whereas (1, 2) appears only for drops at least 14 $\mu$L.

From figure 5, the bands of $(1, 4)_s$ and (1, 4) obviously overlap, as do those of $(1, 3)_s$ and (1, 3). Although the bands of $(1, 2)_s$ and (1, 2) only partially overlap, the overlap increases with the volume of drops. This is presumably because the larger a square drop is, the more it resembles a spherical cap, and hence the closer a square $(1, 2)_s$ behaves like a circular (1, 2).

The shape similarity in figure 4 and frequency band overlap in figure 5 consistently associate $(1, 2)_s$ with (1, 2), $(1, 3)_s$ with (1, 3), and $(1, 4)_s$ with (1, 4). That is, $(1, 2)_s$, $(1, 3)_s$ and $(1, 4)_s$ are the square-drop versions of the (1, 2), (1, 3) and (1, 4), respectively. Large and medium square drops thus resonate like circular drops. This is not surprising.

We have thus far discussed spherical modes of sessile drops only in terms of the three modes in figure 4. These modes are chosen because of their relatively simple shapes and low frequencies. The simple shape facilitates mode identification, especially for the modes deformed by the square footprint. Identifying a complicated mode on a circular drop is already non-trivial. It would be more difficult to identify the same complicated mode disturbed by a square footprint. Modes with lower frequencies are also preferred in these experiments. Low frequency modes exhibit less spectral crowding [22] which means that coexistence and competition of modes are less likely. This favours isolated pure modes and unambiguous modal identification.

In figure 5, the frequency bands of $(1, 2)_s$, $(1, 3)_s$ and $(1, 4)_s$ terminate at larger volumes than those of (1, 2), (1, 3) and (1, 4), respectively. As a square drop's volume decreases, the constraint of footprint geometry gradually prevails in influence over the drop's resonance dynamics. A new family of modes emerge as a result, as described in the following section.

# 4 Grid Modes

Small square drops have free surface deflections that resemble those of a flat and square surface. On a flat surface pinned at $x = 0$, $y = 0$, $x = L$ and $y = L$, any standing wave can be expressed as a 2D Fourier series whose components, or modes, are

$$z_{pq}(x, y, t) = \sin \frac{p\pi x}{L} \sin \frac{q\pi y}{L} \cos(2\pi f_{pq} t) \tag{1}$$

where $p$ and $q$ are any positive integers, and $f_{pq}$ the resonance frequency. Twelve such modes are presented in figure 6. For each mode, the deflection according to equation (1) is rendered as the greyscale map on the left. The brightness represents the local height of the pinned square film. That is, bright and dark regions are peaks and troughs, respectively. On the right is an experimental snapshot of the corresponding mode on a square drop. We denote these modes as *grid modes* since their nodal lines form rectangular grids. A video of selected grid modes is

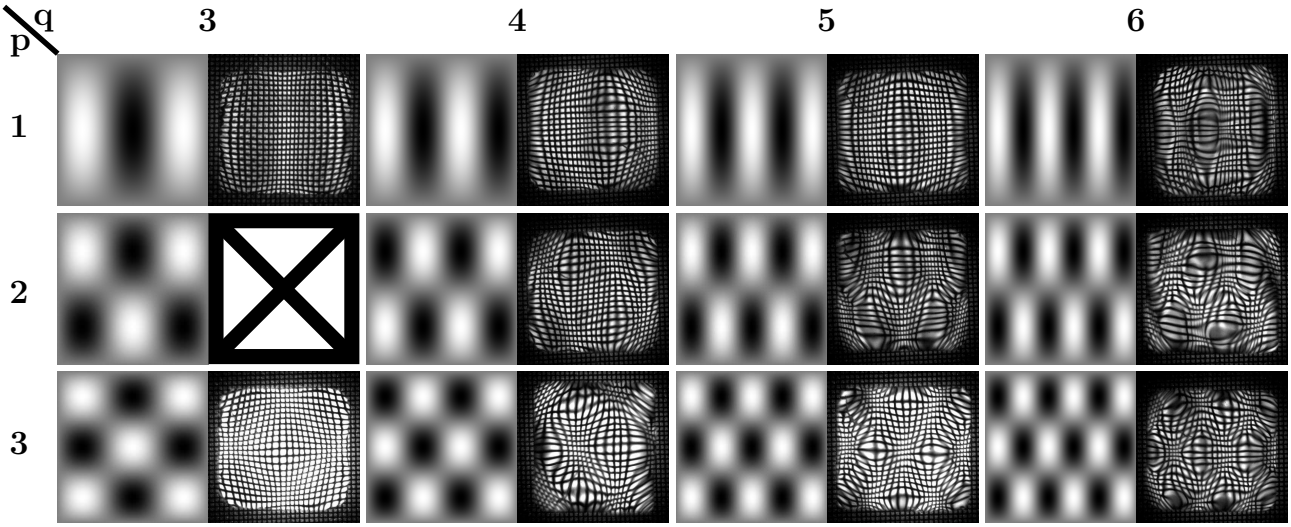


Figure 6: A partial catalog of observed grid modes paired with simulated patterns. For each pair, to the left is shown the mode shape on a pinned, flat square film according to equation (1). The brightness indicates the height. To the right is shown the corresponding snapshot on a square drop, from experiment. The drops are 10 - 16$\mu$L. Among the observations, (1, 3), (1, 5) and (1, 7) are harmonic modes which oscillate at their forcing frequencies. All others are half-frequency subharmonics. Marked with an X as missing is the mode $(p, q) = (2, 3)$ because it has never been observed in our experiments. A video of selected grid modes is provided in our supplementary materials [46].

provided in our supplementary materials [46]. For square drops, we note that $p = q = 1$ cannot occur as it corresponds to a volume oscillation mode.

In our experiments, grid modes appear on small and medium square drops. In the snapshots of figure 6, the mesh is locally magnified if it lies underneath a wave peak. Conversely, the drop's free surface shrinks the mesh wherever it is concave. As an example, $(p, q) = (1, 3)$ shrinks the underlying mesh in the middle but magnifies it to the left and right. Therefore, the instantaneous profile of (1, 3) is a middle trough sandwiched by ridges to the left and right. The corresponding greyscale map also depicts this. Other grid modes can be identified with the same scheme.

We note that, ideally, our square pinning footprint has equal length and width. If this were the case, however, (1, 3) and (3, 1) should resonate at exactly the same frequency and hence coexist or compete. So should any other grid mode and its transposed twin. Relevant observations have been reported by Douady and Fauve [24], in which each mode of a *square* Faraday wave coexists or competes with its transpose depending on the ratio of the two wavelengths. Our experiments are free from such modal interactions, because the length and width of our 'square' pinning footprint differ, if only by approximately 2.5%. This is an imperfection of pin-

ning footprint preparation. However, the imperfection separates the frequency bands of (1, 3) and (3, 1) enough that (1, 3) resonates within a lower frequency range. The slight imperfection also separates other modes from their transposes. Thanks to this imperfection, we are able to observe the isolated pure modes in figure 6.

Few of our grid modes oscillate at the forcing frequency of our mechanical oscillator. In fact, most of them are half-frequency subharmonic modes. Harmonic modes are $(p, q) = (1, 2w - 1)$ and their transposes, where $w$ is any positive integer. In our experiments, the only harmonic modes are (1, 3), (1, 5), (1, 7) and their transposes; all others are half-frequency subharmonics.

Now we characterize the frequencies of grid modes. The six relevant, independent variables are observed frequency $f$, dimensionless wavenumber $\bar{k} \equiv \pi \times \sqrt{p^2 + q^2}$, drop volume $V$, footprint area $A_0$, liquid density $\rho$ and surface tension $\sigma$. For convenience, we replace $A_0$ and $V$ by two length scales $L$ and $H$ as

$$L \equiv \sqrt{A_0}, \quad H \equiv \frac{V}{A_0} \tag{2}$$

which leaves the following list of relevant variables

$$\{f, \bar{k}, H, L, \rho, \sigma\}. \tag{3}$$

Dimensional reasoning leads to scaled frequencies that depend on two groups,

$$(2\pi f)^2 \frac{\rho L^2 H}{\sigma} = Y(\bar{k}, \frac{H}{L}) \tag{4}$$

where $Y$ is an unknown function under construction. To proceed, we assessed the scaling between $f$ and $\bar{k}$ with a least-square fit and obtained $f \sim \bar{k}^{1.965} \approx \bar{k}^2$. Accordingly, we re-write $Y = \bar{k}^4 \times \bar{h} \times (H/L)^n$ where $\bar{h}$ and $n$ are undetermined. For simplicity, we take $n = 1$, which gives

$$f = \frac{1}{2\pi} \sqrt{\frac{\sigma}{\rho L^3} \bar{k}^4 \times \bar{h}}. \tag{5}$$

We then use $\bar{h}$ as a fitting parameter to capture the variation of frequency with drop volume.

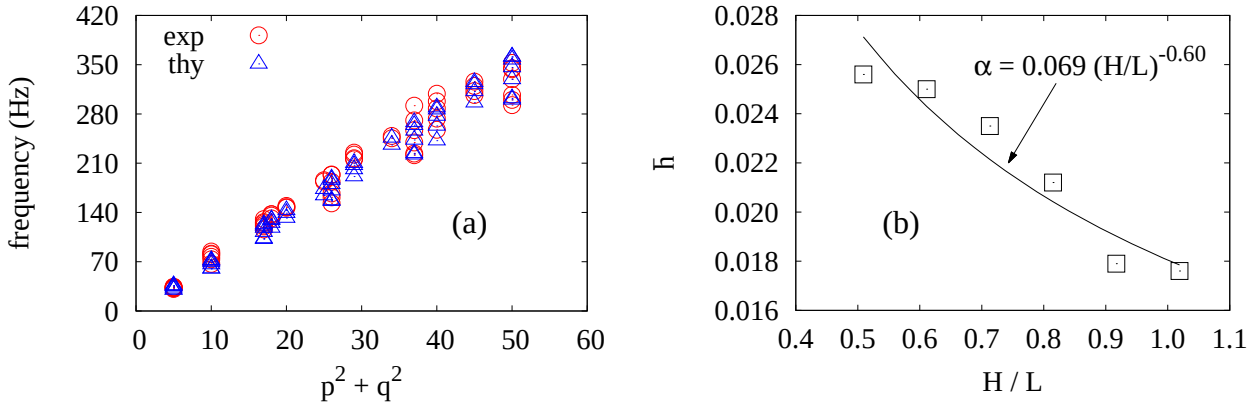


Figure 7: (Color online) Dispersion relation of grid modes for square drops of 10 - 20 $\mu$L. (a) Observed (◯) and predicted (Δ) frequencies. (b) The fitting parameter $\bar{h}$ for different drop volumes.

For our observations of each drop volume, we calculate $\bar{h}$ that minimizes the error function

$$\epsilon(\bar{h}) = \sum_i \left[ f_i - \frac{1}{2\pi}\sqrt{\frac{\sigma}{\rho L^3} \times \bar{h}\bar{k}_i^4} \right]^2. \tag{6}$$

where $f_i$ and $\bar{k}_i$ are the frequency and dimensionless wavenumber of our $i-$th observation. Then we find the scaling $\bar{h} = \bar{h}(H/L) = a \times (H/L)^b$. We note that taking $n = 1$ in equation (4) does not constrain the scaling between frequency $f$ and $H/L$. The true scaling is $f \sim (H/L)^{b/2}$, and the exponent $b$ will be given by our fit.

Figure 7 shows the results of our fit. In figure 7(a), the mean observed frequency (◯) is plotted with the prediction (Δ) from equation (5) for each mode and each drop volume. The experimental data is provided in the supplementary materials [47]. The multiple frequencies for each mode are the observations and the predictions for square drops of different volumes. The average fitting error is by 5.8% with a standard deviation of 4.3%. In figure 7(b), $\bar{h}$ is plotted against $H/L$. A least-square fit suggests $\bar{h} \sim (H/L)^{-0.6}$. Recall that drop volume $V = HL^2$ and $L$ is fixed. Therefore, $\bar{h} \sim (H/L)^{-0.6}$ means $\bar{h} \sim V^{-0.6}$. This is consistent with our observations: the larger the drop volume, the lower the frequency for each grid mode. Finally, we note that in the dimensionless form,

$$\bar{h} = 0.069\left[\frac{H}{L}\right]^{-0.6}. \tag{7}$$

Grid modes are closely related to the natural modes of square Faraday waves. Faraday

waves are capillary-gravity waves generated by plane-normal oscillations of a liquid bath. At rest, the bath is of uniform depth $h$ held in a right cylinder. The observed Faraday waves are those governed by the classical capillary-gravity dispersion relation

$$(2\pi f)^2 = (gk + \frac{\sigma}{\rho}k^3)\tanh(kh), \tag{8}$$

where $g$ is the gravitational acceleration and $k$ the physical wavenumber. In their classical work on Faraday waves, Benjamin and Ursell used these natural frequencies to scale their parametrically forced resonance modes [37]. We shall refer to natural modes with these frequencies as BU modes. In what follows, we shall consider grid and BU modes on a liquid of the same footprint/planform area $A_0$ whenever we compare these modes. BU modes belong to flat free surfaces with a fully mobile contact line and a constant, 90° contact angle. In contrast, grid modes occur on square drops which have curved free surfaces, pinned contact lines and no depth below the contact lines. Despite these differences, the two families of resonance dynamics share common features in their shape and frequency responses. In what follows, we first associate grid and BU modes by shape. Then we compare and contrast how their frequencies scale with wavenumber $k$ and drop volume $V$.

A one-to-one shape correspondence exists between grid and BU modes. For a liquid bath in a right square cylinder, the shapes of BU modes are [37]

$$S_{uv} = \cos\left(\frac{u\pi x}{L}\right)\cos\left(\frac{v\pi y}{L}\right) \tag{9}$$

where $u$ and $v$ are non-negative integers, and $L^2 = A_0$ the bath's planform area. If we compare grid and BU modes with the same indices, equations (1) and (9) lead to

$$(u, v) = (p, q) \quad \text{or} \quad (u, v) = (q, p). \tag{10}$$

We restrict our discussion to BU modes with $u \times v > 1$ since $p \times q > 1$ for our grid modes. For a grid mode and a BU mode related by (10), they have the same dimensionless wavenumbers, and their shapes differ only as sine differs from cosine. This establishes a one-to-one correspondence to uniquely associate each grid modes to a BU mode by shape. A natural next question is how the frequencies of corresponding grid and BU modes compare.

Grid modes exhibit an almost identical dispersion relation as certain BU modes do. Consider equation (8) for BU modes. If the liquid bath is shallow, $\tanh(kh) \approx kh$. Additionally, if capillarity dominates, $\rho g/\sigma k^2 \ll 1$, and equation (8) becomes

$$f = \frac{1}{2\pi}\sqrt{\left(gk + \frac{\sigma}{\rho}k^3\right)\tanh(kh)} \approx \frac{1}{2\pi}\sqrt{\frac{\sigma}{\rho}k^3\tanh(kh)} \approx \frac{1}{2\pi}\sqrt{\frac{\sigma}{\rho}k^4 h} = \frac{1}{2\pi}\sqrt{\frac{\sigma\bar{k}^4}{\rho L^3}\frac{h}{L}}. \qquad (11)$$

This would be identical to equation (5) if we take $\bar{h} = h/L$. In this way, we uniquely associate each grid mode with a BU mode: for any grid mode $(p, q)$ with frequency $f$ on a square drop of 'depth' $H$ and footprint area $A_0$, there exists a BU mode $(u, v) = (p, q)$ that also oscillates at $f$ on a bath of depth $h = \bar{h} \times L$ and planform area $A_0$. Recall that $h$ relates to $H$ as $h = 0.069 \times H^{-0.6} \times L^{0.4}$. Are grid modes simply square Faraday waves transplanted onto a sessile drop?

The answer is no, because the frequencies of grid and BU modes vary with liquid volume in opposite ways. In experiments, each grid mode has a lower frequency on a larger drop. This is a typical *drop-like* behavior reported for experiments with sessile [11, 22, 48], pendent [49] and levitated [50] drops. In contrast, each mode of Faraday waves is known to possess a higher frequency on a deeper bath [27]. Such *bath-like* behavior is not shared by grid modes. Interestingly, grid modes are simultaneously bath-like in shape and frequency-wavenumber scaling but drop-like in frequency-volume scaling. The mixed features suggest grid modes as a family of transitional dynamics between the resonance of sessile drops and liquid baths.

Before proceeding, we note that equation (5) helps us rationalize the absence of (2, 3) mode, cf. figure 6. According to equation (5),

$$f = \frac{1}{2\pi}\sqrt{\frac{\sigma}{\rho L^3} \times \bar{h}\bar{k}^4} = s \times (p^2 + q^2) \qquad (12)$$

where

$$s \equiv \frac{\pi}{2}\sqrt{\frac{\sigma}{\rho L^3} \times \bar{h}}.$$

For each grid mode $(p, q)$, equation (12) means that the forcing frequencies $f^*$ should be

$$f^* = s \times (p^2 + q^2)$$

for harmonic modes and

$$f^* = 2s \times (p^2 + q^2)$$

for half-frequency subharmonic modes. In experiments, observed modes with $p = 2$ or $q = 2$ are half-frequency subharmonics. As such, (2, 3) is presumably half-frequency subharmonic, and the forcing frequency would scale as $2 \times (2^2 + 3^2) = 26$ which equals $1^2 + 5^2$ of (1, 5). Recall that (1, 5) is harmonic. Therefore, (2, 3) and (1, 5) correspond to the same (range of) forcing frequency. In our experiments, however, harmonic modes always require less acceleration to excite. As a result, (1, 5) prevails to dominate the drop's resonance and masks the (2, 3) response.

# 5 Spherical vs. Grid Modes

Spherical modes and grid modes differ in shapes as already discussed with figures 4 and 6. Now we contrast their frequency responses using classical dispersion relations. In this section, the term *wavenumber* refers to dimensionless wavenumber $\bar{k}$ unless otherwise specified.

Here we include data from our prior work [22] and experiments first reported here. All grid modes from new experiments are included, and recall that the wavenumber $\bar{k} = \pi \times \sqrt{p^2 + q^2}$. Among all spherical modes, we only consider zonal and sectoral modes. The first five zonal modes $(n, l)$ = (2, 0), (3, 0), ..., (6, 0) from [22] are considered, and the number of layers $n$ is used as the wavenumber. For sectoral modes, we combine data for $(n, l)$ = (1, 5), (1, 7) and (1, 9) from [22] and $(n, l)$ = (1, 2), (1, 3) and (1, 4) from new experiments, and the number of sectors $l$ is used as the wavenumber. Tesseral modes are excluded owing to the ambiguity in describing such 2D waves with a single wavenumber.

We compare the selected modes by how their frequencies $f$ scale with wavenumber $\bar{k}$. For the comparison, pairs of $(f, \bar{k})$ are least-square fit by $f = \lambda \bar{k}^{\beta}$ for each type of mode and each drop volume $V$. The modes are compared in terms of $\beta$ in figure 8. As an example, the square of $V = 10\mu$L is obtained from fitting all data points $(f, \bar{k})$ for grid modes observed on a $10\mu$L square drop.

According to figure 8, dispersive travelling waves underlie all selected modes. Standing waves can result from the superposition of two counter-progagating waves, as is well known.

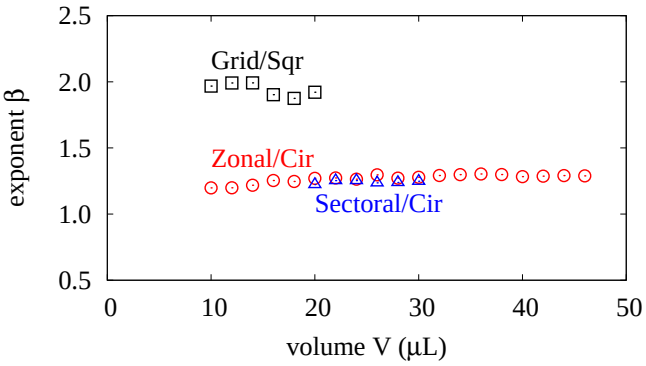


Figure 8: (Color online) Exponent $\beta$ for sessile drop modes. Grid/Sqr: grid modes on square drops. Sectoral/Cir: sectoral modes on circular drops. Zonal/Cir: zonal modes on circular drops.

Recall that a non-dispersive wave has a linear dispersion relation (i.e. $\beta = 1$), and its wavefront travels without distortion [51]. In contrast, a dispersive wave has many phase velocities which depend on the wavelength. As such, the wavefront deforms as it propagates. In figure 8, it's not surprising that all observed modes are dispersive. This is because their wavefronts must adapt to fit the equilibrium drop shapes as they propagate. Spherical modes disperse presumably because their polar waveforms are Legendre functions instead of sine waves. The polar waveforms must deform to conserve the drop's volume as they travel. For grid modes, the wavefronts propagate on surfaces curving both parallel and perpendicular to the wavefront. This means the wavefronts constantly experience variation of liquid depth which refracts the waves and smears the wavefronts.

Figure 8 also indicates distinct dispersions for grid and spherical modes. The difference apparently trends with how their wavefronts smear. Spherical modes possess sinusoidal azimuthal waves which do not deform as they propagate. They are dispersive *only* in the polar direction. In contrast, the wavefronts of grid modes are constantly smeared *both* parallel and perpendicular to the direction of propagation. Consequently, the *one-dimensionally dispersive* spherical modes disperse much less than grid modes which are *two-dimensionally dispersive*.

A final remark on dispersion: figure 8 is consistent with our prior work [21] for zonal and sectoral modes. Namely, the resonance frequency does not scale with wavenumber as Rayleigh-Lamb theory would predict ($f \sim \bar{k}^{1.5}$) [38, 39]. In figure 8, $\beta$ of zonal and sectoral modes varies between 1.22 and 1.26 but never approaches 1.5. This agrees with the overprediction of Rayleigh-Lamb theory already reported [21] where Rayleigh-Lamb predictions are tested only

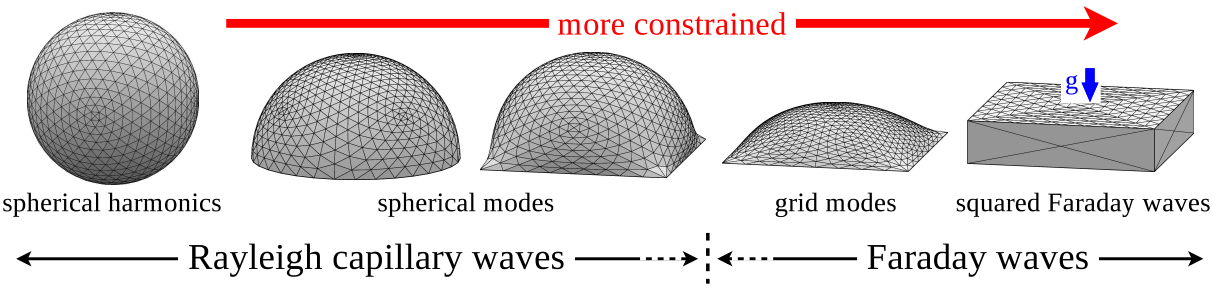


Figure 9: (Color online) Continuum of rest shapes with corresponding resonance modes labeled below. From spherical harmonic waves on free drops, Rayleigh capillary waves [38], to rectangular waves on flat surfaces in rectangular containers, Faraday waves [13]. The dashed line segments denote the transition between spherical and grid modes at contact angles of approximately 75° - 85°.

for drops of one volume and a limited range of contact angles. Figure 8 further validates the conclusion for a broader range of the parameters.

Contrasting observation of grid and spherical modes reveals the different extents to which the square footprint influences a drop's resonance. Our large square drops resemble spherical caps and exhibit spherical modes. This means that large square drops resemble large circular drops both statically and dynamically, which in turn implies an insignificant effect of footprint geometry for large sessile drops. As such, spherical modes are mainly the consequence of a dominating capillary force. For the same reason, these modes can be regarded as a sessile drop's *characteristic*. In contrast, our small square drops resemble flat square surfaces and perform grid modes. However, small circular drops remain spherical caps and perform spherical modes [22]. The difference highlights the dominant effect of footprint geometry over capillary force for small square drops. As such, grid modes are a footprint-influenced, *constrained response*. Finally, our medium square drops exhibit both spherical and grid modes and suggests comparable influences of capillarity and footprint geometry. A gradual transition between the two families of modes occurs. A main result of this paper is the determination of the transition regime to be 75° - 85° in terms of a square drop's contact angle (cf. appendix).

Responses can be related to Rayleigh capillary and Faraday waves. With figure 9, we consider the resonance of a liquid under different extents of constraint by a support. Unconstrained free drops form spheres, and their natural modes are spherical harmonics [38, 39]. Spherical harmonics can thus be thought of as the free drop characteristic, because they occur solely due to the drop's inertia and surface tension without any constraint. A free drop becomes a circular drop if it is brought in contact with a homogeneous substrate. The constraint of the

substrate modifies the drop's resonance spectrum [21] such that its natural modes are no longer spherical harmonics but what we here call spherical modes. As discussed, these modes occur when capillary force dominates and effects of footprint geometry are insignificant. We have identified spherical modes as the characteristic of sessile drops. Relative to the Rayleigh free drop, however, spherical modes are also a constrained response because they are influenced by the substrate presence.

Our square pinning footprint constrains square drops not only with a liquid-solid contact, but also with a footprint symmetry exotic to the Rayleigh drop. As such, our large square drops show spherical modes with fixed azimuthal orientations. Planform selects orientation as well as wavenumber in this case. These spherical modes are in fact the sessile drop characteristic with a 'square accent.' For small square drops, the footprint constraint dictates the drop's resonance. Grid modes appear as a result. Our characterization has enabled one to quantitatively associate grid modes with square Faraday waves. Overall, our square drop experiments provide a link between Rayleigh capillary waves and Faraday waves. To summarize, figure 9 presents a continuum of surface waves for liquid drops under different extents of constraint.

# 6 Conclusion

In this work, resonance of square drops is experimentally examined in terms of the shape and frequency responses. Depending on volume, a square drop exhibits either spherical modes like a circular drop or grid modes like a flat square surface. The spherical modes on square drops are identified by comparing their shapes and frequencies with resonating circular drops [12, 22]. For grid modes, ways to identify their shapes and predict their frequencies are proposed. The absence of (2, 3) mode is also rationalized using this viewpoint. These modes are further associated with square Faraday waves. Our subsequent discussion on dispersion quantitatively distinguishes spherical and grid modes. We then compare the overlap of modes to identify spherical modes as a characteristic of sessile drops whereas grid modes as a constrained response of square drops. Finally, we discuss constrained response in a broader context. We end up ordering resonance of different drops into a continuum by the varying extent by which the drops are constrained.

The experiments reported here may be viewed as probing a 2-parameter continuum of driven

droplet resonance problems. Footprint geometry can be continuously deformed from a circular to a square shape. Independently, droplet volume can be varied to yield drop heights from shallow to fat. The endpoint problems of the spherical cap drop with circular planform and the square bath with flat surface have traditionally be modeled somewhat differently. The resonance of driven circular drops has been successfully modeled as a linear stability problem with time-independent coefficients (free response) while the resonance of driven Faraday baths has been successfully modeled as a linear stability problem with time-dependent coefficient (parametric response) leading to a Mathieu-type equation wherein the forcing amplitude appears as parameter. Clearly, a modeling framework that encompasses both extremes is needed. A successful encompassing theoretical framework would answer the question: for a specified footprint, drop volume and amplitude of excitation, will a particular mode respond harmonically or subharmonically? We have demonstrated that, when both are possible, harmonic dominates subharmonic response consistent with the larger excitation amplitude needed for subharmonics. One also expects a cross-over from harmonic to subharmonic response for any particular mode as one deforms in the direction of the driven Faraday bath. These are open questions, however.

We conclude by answering our motivating question. Capillary force and footprint constraint compete to determine a sessile drop's driven response at resonance. Different surface waves arise accordingly. For square drops, a dominating effect of footprint constraint leads to grid modes; otherwise, the drops exhibit spherical modes, the characteristic of sessile drops.

# 7 Acknowledgement

The authors thank Dr. MY Louge for supplying the VTS-100 oscillator and Mr. G. Swan, Dr. B Land, Mr. D Hartino, Dr. SJ Weinstein, Dr. MY Louge, Dr. AT Zehnder, Dr. WH Sachse, Dr. K Boettcher, Dr. C Cohen and Dr. D Lee for assistance and helpful discussions. CT Chang thanks Dr. P Ehrhard for sponsoring his research stay at Technical University Dortmund. The authors also thank the reviewers for their numerous helpful suggestions. Finally, the authors thank NASA (grant no. NNX09AI83G), National Science Foundation (grant no. CBET-1236582) and Xerox Corporation for financial support.

# 8 Appendix

Figure 10 relates a sessile drop's volume and contact angle. For a square drop, the contact angle is calculated at the midpoint of the drop's edge, where it is least affected by the squared corners. It is obtained by finding the drop's meridian profile with Surface Evolver [52], fitting the first 10 points from the endpoint to a polynomial, and calculating the slope at the endpoint. The contact angles for circular drops are calculated analytically for spherical caps, i.e. assuming zero gravity.

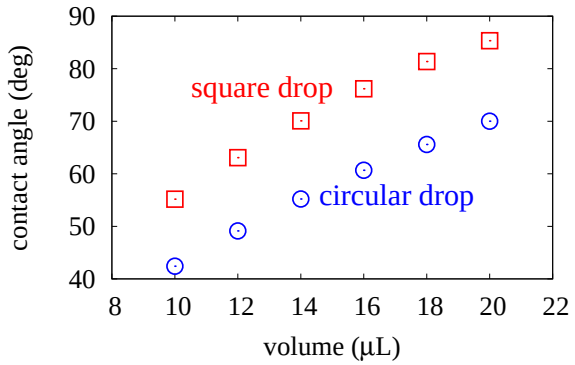


Figure 10: (Color online) Variations of contact angle with the volume of a sessile drop. For square drops, the contact angle is calculated at the midpoint of a square drop's edge.

# References

[1] S. Daniel, M. K. Chaudhury, and J. C. Chen. Fast drop movements resulting from the phase change on a gradient surface. *Science*, 291(5504):633–636, 2001.

[2] S. Daniel, M. K. Chaudhury, and P.-G. de Gennes. Vibration-actuated drop motion on surfaces for batch microfluidic processes. *Langmuir*, 21(9):4240–4248, 2005. PMID: 15836001.

[3] J. Rafael Castrejon-Pita, W. R. S. Baxter, J. Morgan, S. Temple, G. D. Martin, and I. M. Hutchings. Future, opportunities and challenges of inkjet technologies. *Atomization and Sprays*, 23(6):541–565, 2013.

[4] A. Qi, L. Yeo, J. Friend, and J. Ho. The extraction of liquid, protein molecules and yeast cells from paper through surface acoustic wave atomization. *Lab Chip*, 10:470–476, 2010.

[5] P. H. Wright and J. R. Saylor. Patterning of particulate films using faraday waves. *Review of Scientific Instruments*, 74(9):4063–4070, 2003.

[6] R. Shilton, M. K. Tan, L. Yeo, and J. R. Friend. Particle concentration and mixing in microdrops driven by focused surface acoustic waves. *Journal of Applied Physics*, 104(1):–, 2008.

[7] J. Whitehill, A. Neild, T. W. Ng, and M. Stokes. Collection of suspended particles in a drop using low frequency vibration. *Applied Physics Letters*, 96(5):–, 2010.

[8] M. Lee, Y. S. Chang, and H.-Y. Kim. Drop impact on microwetting patterned surfaces. *Physics of Fluids*, 22(7), 2010.

[9] P. Tsai, R. C. A. van der Veen, M. van de Raa, and D. Lohse. How micropatterns and air pressure affect splashing on surfaces. *Langmuir*, 26(20):16090–16095, 2010. PMID: 20860398.

[10] H. Kim, C. Lee, M. H. Kim, and J. Kim. Drop impact characteristics and structure effects of hydrophobic surfaces with micro- and/or nanoscaled structures. *Langmuir*, 28(30):11250–11257, 2012. PMID: 22746551.

[11] A. Lasek H. Rodot, C. Bisch. Zeor-gravity simulation of liquids in contact with a solid surface. *Acta Astronautica*, 6:1083, 1979.

[12] J. B. Bostwick and P. H. Steen. Dynamics of sessile drops. part 1. inviscid theory. *Journal of Fluid Mechanics*, 760:5–38, 12 2014.

[13] M. Faraday. On a peculiar class of acoustical figures; and on certain forms assumed by groups of particles upon vibrating elastic surfaces. *Philosophical Transactions of the Royal Society of London*, 121:299–340, 1831.

[14] R. W. Smithwick III and J. A. M. Boulet.

[15] N. Yoshiyasu, K. Matsuda, and R. Takaki. Self-induced vibration of a water drop placed on an oscillating plate. *Journal of the Physical Society of Japan*, 65(7):2068–2071, 1996.

[16] H. Azuma and S. Yoshihara. Three-dimensional large-amplitude drop oscillations: experiments and theoretical analysis. *Journal of Fluid Mechanics*, 393:309–332, 8 1999.

[17] X. Noblin, A. Buguin, and F. Brochard-Wyart. Vibrated sessile drops: Transition between pinned and mobile contact line oscillations. *The European Physical Journal E*, 14(4):395–404, 2004.

[18] B. Vukasinovic, M.K. Smith, and A. Glezer. Dynamics of a sessile drop in forced vibration. *J. Fluid Mech.*, 587:395–423, 2007.

[19] X. Noblin, A. Buguin, and F. Brochard-Wyart. Vibrations of sessile drops. *The European Physical Journal Special Topics*, 166(1):7–10, 2009.

[20] J. S. Sharp, D. J. Farmer, and J. Kelly. Contact angle dependence of the resonant frequency of sessile water droplets. *Langmuir*, 27(15):9367–9371, 2011.

[21] C.-T. Chang, J. B. Bostwick, P. H. Steen, and S. Daniel. Substrate constraint modifies the rayleigh spectrum of vibrating sessile drops. *Phys. Rev. E*, 88:023015, Aug 2013.

[22] C.-T. Chang, J. B. Bostwick, S. Daniel, and P. H. Steen. Dynamics of sessile drops. part 2. experiment. *Journal of Fluid Mechanics*, 768:442–467, 4 2015.

[23] S. Ciliberto and J. P. Gollub. Chaotic mode competition in parametrically forced surface waves. *Journal of Fluid Mechanics*, 158:381–398, 9 1985.

[24] S. Douady and S. Fauve. Pattern selection in faraday instability. *EPL (Europhysics Letters)*, 6(3):221, 1988.

[25] S. Douady. Experimental study of the faraday instability. *Journal of Fluid Mechanics*, 221:383–409, 12 1990.

[26] W. S. Edwards and S. Fauve. Patterns and quasi-patterns in the faraday experiment. *Journal of Fluid Mechanics*, 278:123–148, 11 1994.

[27] D. Binks, M.-T. Westra, and W. van de Water. Effect of depth on the pattern formation of faraday waves. *Phys. Rev. Lett.*, 79:5010–5013, Dec 1997.

[28] C. Wagner, H. W. Müller, and K. Knorr. Crossover from a square to a hexagonal pattern in faraday surface waves. *Phys. Rev. E*, 62:R33–R36, Jul 2000.

[29] A. Kudrolli, Mathew C. Abraham, and J. P. Gollub. Scarred patterns in surface waves. *Phys. Rev. E*, 63:026208, Jan 2001.

[30] B. A. Puthenveettil and E. J. Hopfinger. Evolution and breaking of parametrically forced capillary waves in a circular cylinder. *Journal of Fluid Mechanics*, 633:355–379, 8 2009.

[31] J. Rajchenbach, D. Clamond, and A. Leroux. Observation of star-shaped surface gravity waves. *Phys. Rev. Lett.*, 110:094502, Feb 2013.

[32] B. Batson, F. Zoueshtiagh, and R. Narayanan. The faraday threshold in small cylinders and the sidewall non-ideality. *Journal of Fluid Mechanics*, 729:496–523, 8 2013.

[33] A. James, B. Vukasinovic, M. K. Smith, and A. Glezer. Vibration-induced drop atomization and bursting. *J. Fluid Mech.*, 476:1–28, 2003.

[34] I. Shani, G. Cohen, and J. Fineberg. Localized instability on the route to disorder in faraday waves. *Phys. Rev. Lett.*, 104:184507, May 2010.

[35] H. Xia, T. Maimbourg, H. Punzmann, and M. Shats. Oscillon dynamics and rogue wave generation in faraday surface ripples. *Phys. Rev. Lett.*, 109:114502, Sep 2012.

[36] J. Miles and D. Henderson. Parametrically forced surface waves. *Annual Review of Fluid Mechanics*, 22(1):143–165, 1990.

[37] T. B. Benjamin and F. Ursell. The stability of the plane free surface of a liquid in vertical periodic motion. *Proceedings of the Royal Society of London. Series A. Mathematical and Physical Sciences*, 225(1163):505–515, 1954.

[38] Lord Rayleigh. On the capillary phenomena of jets. *Proceedings of the Royal Society of London*, 29(196-199):71–97, 1879.

[39] H. Lamb. *Hydrodynamics*. Cambridge University Press, Cambridge, UK, 1932.

[40] K. Kumar and L. S. Tuckerman. Parametric instability of the interface between two fluids. *Journal of Fluid Mechanics*, 279:49–68, 11 1994.

[41] W. Zhang and J. Vi nals. Pattern formation in weakly damped parametric surface waves. *Journal of Fluid Mechanics*, 336:301–330, 4 1997.

[42] A. C. Skeldon and J. Porter. Scaling properties of weakly nonlinear coefficients in the faraday problem. *Phys. Rev. E*, 84:016209, Jul 2011.

[43] A. C. Skeldon and A. M. Rucklidge. Can weakly nonlinear theory explain faraday wave patterns near onset? *Journal of Fluid Mechanics*, 777:604–632, 8 2015.

[44] J. Rajchenbach and D. Clamond. Faraday waves: their dispersion relation, nature of bifurcation and wavenumber selection revisited. *Journal of Fluid Mechanics*, 777:R2 (12 pages), 8 2015.

[45] See Supplemental Material at [file name: SphModeVideo20161010.mp4, URL to be inserted by publisher] for videos of the spherical modes in figure 4.

[46] See Supplemental Material at [file name: GrdModeVideo20161010.mp4, URL to be inserted by publisher] for videos of selected grid modes observed in our experiments.

[47] See Supplemental Material at [file name: GridModesData.xls, URL to be inserted by publisher] for the raw data of observed grid modes.

[48] M. Perez, Y. Brechet, L. Salvo, M. Papoular, and M. Suery. Oscillation of liquid drops under gravity: Influence of shape on the resonance frequency. *EPL (Europhysics Letters)*, 47(2):189, 1999.

[49] H. M. Jong, H. K. Byung, and H.-Y. Kim. The lowest oscillation mode of a pendant drop. *Physics of Fluids*, 18(2):021702, 2006.

[50] C. L. Shen, W. J. Xie, and B. Wei. Parametrically excited sectorial oscillation of liquid drops floating in ultrasound. *Phys. Rev. E*, 81:046305, Apr 2010.

[51] A. R. Seebass S. Leiboich. *Nonlinear Waves*. Cornell University Press, Ithaca and London, 1974.

[52] See Supplemental Material at [file name: SqrDropCalc.fe, URL to be inserted by publisher] for our Surface Evolver source code.